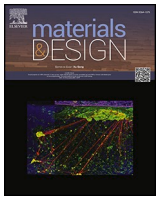
Materials & Design 244 (2024) 113138



Contents lists available at ScienceDirect

Materials & Design

journal homepage: www.elsevier.com/locate/matdes



Grain refinement of magnesium castings using recycled machining chips

Xinyi Hao [a], Zhuocheng Xu [a], Christopher M. Gourlay [b], Qianqian Li [a,*]

[a] Department of Aeronautics, Imperial College London, London SW7 2AZ, UK
[b] Department of Materials, Imperial College London, London SW7 2AZ, UK

A B S T R A C T

A simple and effective recycling approach of magnesium alloys can offer economic and environmental benefits. This study demonstrates that by simply remelting AZ91/AZ80 machining chips and shape casting, the tensile properties of the castings can be preserved and substantial grain refinement can be achieved, compared to casting from ingots using the same alloy. Cooling curves for the samples, obtained through the immersion thermocouple method, showed that nucleation event density in chip melts consistently exceeds that in ingot melts, particularly at low undercoolings. Tensile tests showed that chip castings exhibit a slightly higher 0.2% proof stress than castings from ingots, with increases of 5% and 1% for as-cast and solution-treated conditions, respectively, due to the Hall-Petch effect. Elongation to fracture was similar for both chip and ingot samples, with fractography indicating entrainment defects, rather than grain size, predominantly determined this outcome. These combined results indicate that the shape casting of AZ91/AZ80 machining chips could be used as part of the closed-loop recycling of magnesium.

1. Introduction

Alloy recycling is a crucial pathway to drive the transition towards a circular economy, ultimately contributing to achieving net-zero emissions by 2050, as it can significantly reduce the consumption of raw materials and energy and decrease greenhouse gas emissions. Magnesium (Mg) alloys, as the lightest structural metals, have been widely used in the automotive and aerospace industries, contributing to increased energy efficiency and reduced carbon emissions. However, primary Mg production is energy-intensive, which may offset the benefits associated with utilizing magnesium parts [1]. The energy required for recycling Mg is only 5 % of that needed to produce an equivalent weight of primary Mg [2–4], underscoring the need to expand Mg recycling for both economic and environmental gain.

Among all magnesium alloys, the AZ series containing Al and Zn is the most widely used [5]. Mg-9Al-0.7Zn-0.2Mn (wt%) is particularly favoured due to its balance of mechanical properties and corrosion resistance [6]. It is referred to as AZ91 when used for casting [7] and AZ80 for forgings [8], with the former commonly employed for thin-walled integrated automotive components [9] and the latter for advanced automotive wheels [9,10]. Both applications generate chips during machining. For example, the chips produced by the machining of die-castings account for approximately 7 % of the final part's weight [11], whereas this percentage can be greater for forgings. Therefore, recycling these chips holds significant potential.

For magnesium alloy scrap, which encompasses trimmings, chips, and rejected parts, conventional recycling primarily uses chemical methods, including flux or fluxless refining and hydrometallurgical processes [2,12]. Specifically for chip recycling, extrusion has been proposed as a solid-state technique [13]. The benefits are that it prevents oxidation during recycling and results in material with a fine grain size, enhancing strength and ductility [14]. This technique is especially apt for recycling mixed chips of magnesium alloys and aluminium alloys to produce alloys that are challenging to cast directly (e.g. AJ62 mixed with A390) [11]. However, its limitations include the production of only elongated components with specific cross-sectional shapes and the long duration of the entire process cycle [15]. Another technique that utilizes chips for processing Mg alloys is thixomolding. This semi-solid processing technique uses granules obtained by mechanically comminuted ingots as feedstock material, enabling the production of net-shape components with complex geometries [16]. However, thixomolding does not usually use recycled machining chips. In contrast, directly remelting and shape casting could be a simple and efficient method for recycling clean magnesium alloy chips, yet there is limited research reported on this subject. Since casting has consistently been the primary manufacturing method for magnesium alloy components, accounting for approximately 98 % of magnesium structural applications [17], recycling chips of AZ91 and AZ80 through shape casting could broaden their application potential.

To verify the quality and usability of castings made from chips, two key factors must be considered. Firstly, it is necessary to ascertain whether a fine grain size can be obtained without the addition of grain refiners. A small grain size is desirable for magnesium alloy casting since it usually improves both processability and performance. For example,

* Corresponding author.
E-mail address: Qianqian.li@imperial.ac.uk (Q. Li).

https://doi.org/10.1016/j.matdes.2024.113138
Received 2 May 2024; Received in revised form 18 June 2024; Accepted 2 July 2024
Available online 3 July 2024
0264-1275/© 2024 The Authors. Published by Elsevier Ltd. This is an open access article under the CC BY license (http://creativecommons.org/licenses/by/4.0/).

during casting, a small grain size reduces casting defects [18] and hot tearing susceptibility [19] and, during subsequent deformation processing, it improves the microstructure uniformity and formability [20–23]. In service, a small grain size provides grain boundary strengthening [24,25] and can also improve corrosion resistance through finely dispersed β-$Mg_{17}Al_{12}$ phase particles [26,27]. However, grain refinement in Mg-Al based alloy castings remains a challenge. Mg-Zr master alloys, as the sole commercial grain refiner for magnesium alloys at present [23], are ineffective for alloys containing Al, Si, and Mn due to the formation of stable intermetallic phases[28,29]. Although extensive studies have been conducted on the grain refinement of magnesium alloys [25,28–32], there remains an ongoing need for improved grain refinement approaches for Mg-Al alloys. One approach developed in recent years [23,33] achieved grain refinement in cast AZ91 through an intensive melt shearing technique and attributed this to the role of dispersed magnesium oxide (MgO) particles. Considering the presence of natural MgO on the surfaces of machining chips and their high surface area to volume ratio, it is interesting to explore if using recycled machining chips as feedstock for shape casting has any grain refinement effect.

Another factor is whether the native MgO on machining chip surfaces might have a detrimental effect on the quality of castings produced from remelted chips. It is widely reported [34–40] that introducing the oxide layer from the surface of molten magnesium into the melt can lead to the formation of damaging entrainment defects. These defects act as pre-existing cracks in the castings, which may result in a significant reduction in fracture toughness and ductility. Thus, evaluating the tensile properties and oxide defects of castings made from chips versus from ingots is necessary.

Therefore, this study uses the grain size and tensile performance of castings as metrics to study the feasibility of recycling AZ91/AZ80 chips via a direct shape casting route. First, the grain size of castings made from chips and ingot feedstock under different cooling rates is compared, with cooling curves being utilised to analyse the distribution of nucleation events. Then, the tensile performance of castings made from chips and ingot feedstocks, both in as-cast and solution-treated states, is examined, and fractography and defect analysis are conducted to assess whether the large surface-to-volume ratio of chips adversely affects tensile performance.

2. Experimental

The starting materials, both chips and ingots, were commercial alloys supplied by Non Ferrum GmbH, with a composition of 8.67 wt% Al, 0.60 wt% Zn, 0.26 wt% Mn, and 0.03 wt% Si. According to ASTM standards [7,8], this composition lies within the overlapping region of AZ91 and AZ80 alloys. The chips were machined from the same batch of ingots using a cutting mill, in ambient air without applying any coolant or lubricant, and their size distribution, determined by sieve analysis according to ISO 4497 [41], is shown in Table 1. Fig. 1 shows the morphology of the as-received chips at different magnification levels, with Fig. 1(a) displaying the macroscopic morphology of the chips and Fig. 1(b) showing representative external surfaces of the chips. The shapes of the chips include granular and saw-tooth forms, attributable to varying cutting speeds, with the granular form typically corresponding to higher cutting speeds than the saw-tooth form [42]. Additionally, each chip features a smooth rake face and rough, sometimes saw-toothed, flank faces, with their microscopic morphologies shown in Fig. 1(c) and (d). In Fig. 1(e), energy-dispersive X-ray spectroscopy (EDX) elemental analysis shows that some of the particles are oxides, while the majority of the areas do not exhibit detectable levels of oxygen.

Table 1
Size distribution of chips.

Size distribution	Value
> 4000 μm	0.0 %
> 3150 μm	0.6 %
1000–1400 μm	31.2 %
< 1000 μm	4.8 %
< 710 μm	0.3 %

For gravity casting, 120 g of the alloy was placed into a mild steel crucible, heated to 680 °C, and held at this temperature for 30 min in a resistance furnace under an argon atmosphere. Subsequently, the molten alloy was poured into a steel mould (Mould I), which was pre-heated to 200 °C, producing cylindrical rods with a diameter of 12 mm and a length of 15 cm. To record cooling curves, a K-type thermocouple was pre-fixed within Mould I, with its tip positioned at the centre of the cross-section of the cast rod, 10 cm above the base. Cooling curves were recorded using a Keysight 34972A data acquisition system at a frequency of approximately 23 Hz.

Another steel mould (Mould II) was used to cast tensile specimens (overall dimensions: Φ17 mm × 100 mm) and compression rods (Φ13.5 mm × 100 mm), requiring slight stirring to ensure thorough melting of the alloy before casting due to its complex cavity shape. 180 g of the alloy was heated to 680 °C using the same equipment and methods as described above and held for 25 min. Subsequently, a truncated conical stirrer was inserted into the molten alloy and stirred at 60 RPM. The maximum Reynolds number in the liquid during the stirring process was estimated to be around 1×10^3, suggesting that it largely remained within the laminar flow regime. After 5 min of stirring, the stirrer was withdrawn, and the molten alloy was poured into Mould II, which was preheated at 200 °C, once the melt had stopped spinning.

For the slow cooling experiments, 180 g of the alloy was heated to 700 °C and held for 30 min. Then, the crucible was removed from the furnace and placed in ambient air. A K-type thermocouple was immediately inserted into the molten alloy, with its tip positioned at the centre of the cross-section, approximately 1.5 cm above the bottom of the crucible (the melt depth was about 3 cm). An insulating board was placed on top of the crucible to prevent ignition of the alloy. Cooling curves were recorded using a Pico Technology TC-08 thermocouple data logger with a sampling rate of 5 Hz.

Throughout these processes, the crucible, stirrer, and both moulds were pre-coated with boron nitride aerosol spray from Precision Ceramics. All thermocouples were calibrated with commercial-purity aluminium before and after use, and the error did not exceed 0.5 °C.

For tensile testing, the tensile rods were cut off from Mould II castings. Some tensile rods were tested in the as-cast condition and others were subjected to T4 solution heat treatment before tensile testing. For solutionising, specimens were exposed to a temperature of 410 ± 4 °C in a forced-air convection oven for a duration of 20 h, followed by a water quenching process, in compliance with the ASTM B661 standard [43]. The density of the tensile specimens was measured using the Archimedes method specified in ASTM B962 [44] before the tensile test, and the volumetric porosity of the specimens was computed by comparing it to the density of a hot-rolled AZ91 sample, considered as void-free (with a density of 1.81 g/cm^3). Subsequently, tensile tests were performed on both cast and heat-treated specimens, following the ASTM B557M standards [45]. Tensile testing was performed using an Instron 5969 universal testing machine at a strain rate of $1.0 \times 10^{-3}s^{-1}$ where strain was measured using strain gauges. A minimum of 6 tensile specimens was tested under each condition to ensure the repeatability of the results.

For metallographic preparation, cross-sections close to thermocouples or fracture faces were selected, and the sampling locations for chip and ingot samples were kept consistent. These samples were ground sequentially with SiC abrasive papers of 1200, 2000, and 4000 grit with water, followed by polishing to a mirror-like finish using an ethanol-diluted colloidal silica suspension. Subsequently, an etching method adapted from reference [46] was employed, where the samples were stirred in an etching solution composed of glacial acetic acid, deionised

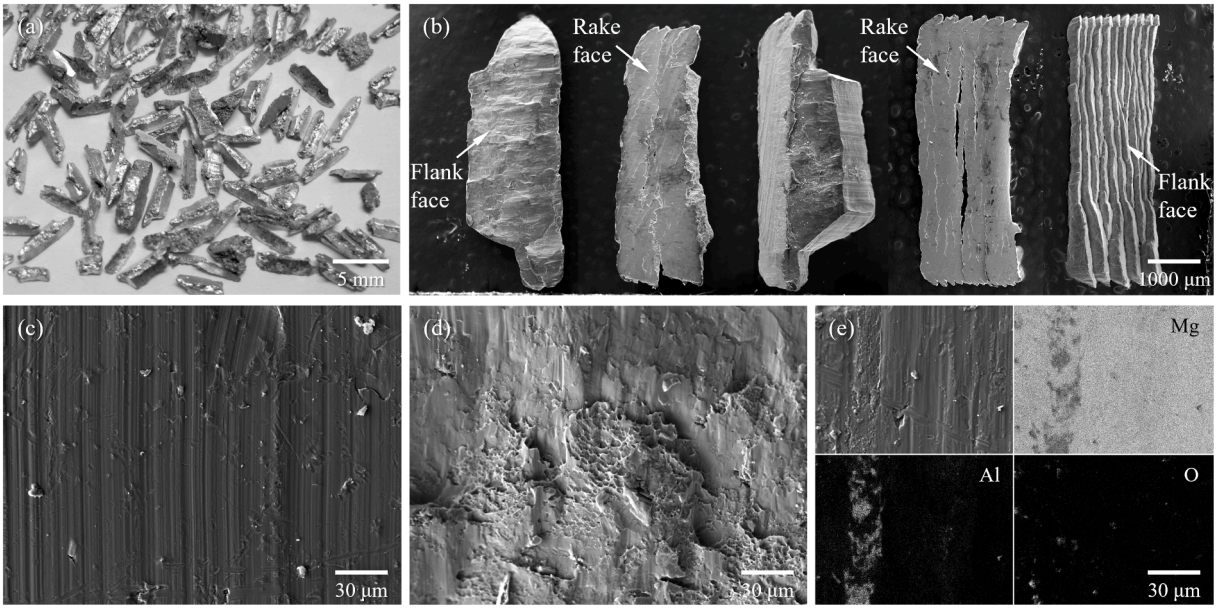


Fig. 1. (a) Macroscopic morphology of as received AZ91 machining chips, (b) representative external surfaces of chips, (c) microscopic morphology of the rake face, (d) microscopic morphology of the flank face, and (e) EDX surface mapping.

water, and anhydrous ethanol in a ratio of 1:44:156 for 100 to 200 s. The samples were then rinsed with anhydrous ethanol, and the surface was dried with compressed air.

For microstructure characterisation, an Olympus BX53M optical microscope equipped with polarised light and a retardation wave plate was utilised to inspect the grain morphology of the etched samples. The average grain size of α-Mg in each sample was measured using the linear intercept method, following the ASTM E112 standard [47]. Secondary dendrite arm spacing (SDAS) was measured using the linear intercept method recommended by Ref [48]. The fracture morphology was captured using a Hirox HRX-01 microscope fitted with a high-range turret zoom lens HR-2500(E), and the images obtained were analysed with ImageJ software to measure the area fraction of defects on the fracture surfaces. Observation and analysis of chips, polished planes, and fracture surfaces were conducted using a Zeiss AURIGA scanning electron microscope (SEM), which was furnished with an Oxford Instruments INCA x-sight energy-dispersive X-ray spectroscopy (EDX) detector.

3. Result and discussion

3.1. Grain refinement effect from chips feedstock

In this work, we discovered that using recycled chips as feedstock resulted in substantial grain refinement during casting. For slow-cooled samples with a liquid cooling rate of 0.7 °Cs^{-1} (between 650 °C and 630 °C), the grain size of chip samples (300 ± 18 μm) was reduced by 84 % compared to ingot samples (1879 ± 76 μm). As the liquid cooling rate increased to 87 °Cs^{-1}, unstirred gravity-cast chips exhibited a grain size (142 ± 8 μm) decrease of approximately 50 % relative to ingot samples (286 ± 43 μm). The same grain refinement effect was also observed in castings from Mould II, where chip castings always exhibited smaller grain sizes than castings from ingots cast under the same conditions. The specific grain sizes are shown in Fig. 2, where (a) to (d) display optical microscope images of etched samples from slow-cooled and gravity-casting processes, and (e) summarises the average grain sizes and standard deviations for each condition, with each group containing at least six samples.

The grain size of ingot samples exhibited a strong sensitivity to the cooling rate, being significantly reduced from 1879 ± 76 μm in slow cooling (0.7 °Cs^{-1}) to 286 ± 43 μm in gravity casting (87 °Cs^{-1}). In contrast, the fine grains in chip samples demonstrated a weaker dependence on the cooling rate, only reducing from 300 ± 18 μm to 142 ± 8 μm, as evident from two additional comparisons. Firstly, in Fig. 2(b) and (d), there is a larger variation in grain size from the edge to the centre in ingot samples. Another piece of evidence comes from the last two groups in Fig. 2(e), which were sampled from different rods of the same castings. As they were sharing an identical melt, the variations in grain size can be attributed exclusively to disparities in cooling rate and flow conditions, with the former being inversely correlated with casting diameter. The sampling cross-section of the compression rod has a diameter of 13.5 mm, whereas the tensile rod is 8.6 mm. For reference, the diameter of the mould I casting is 11.9 mm.

Despite differences in grain size, chip samples and ingot samples with the same cooling conditions show highly similar secondary dendrite arm spacing (SDAS). Using micrographs such as those in Fig. 3, the average SDAS are 14.9 ± 0.7 μm and 15.1 ± 0.4 μm for gravity-cast chip and ingot samples, respectively, and 64.7 ± 1.5 μm and 64.8 ± 1.9 μm for slow-cooled chip and ingot samples, respectively. These similarities indicate highly similar cooling rates within each experimental set for both chips and ingots due to the relationship between SDAS (λ_2) and the local freezing time (Δt) [49], which can be simplified as Eq. (1), and has been confirmed to be approximately valid for AZ91 [50–55].

$$\lambda_2 \propto (\Delta t)^{1/3}$$

3.2. Thermal analysis of solidification process

To analyse the effects of chip feedstock on α-Mg nucleation, cooling curves for both chips and ingots were recorded during unstirred slow cooling and unstirred gravity casting, as illustrated in Fig. 4. Three parameters were measured for cooling curve analysis: (i) the cooling rate in the liquid between 650 °C and 630 °C; (ii) the minimum temperature before recalescence, T_{min}; and (iii) the temperature rise of recalescence. Experiments were repeated six times for each condition, and the parameters are presented in Table 2. In both solidification conditions, it can be observed that chips and ingots shared the same cooling rate, and that chips consistently exhibited higher T_{min} and smaller recalescence compared to ingots. The difference between chips and ingots is the largest for slow cooling. It is also clear in Fig. 4 and Table 2 that, as the

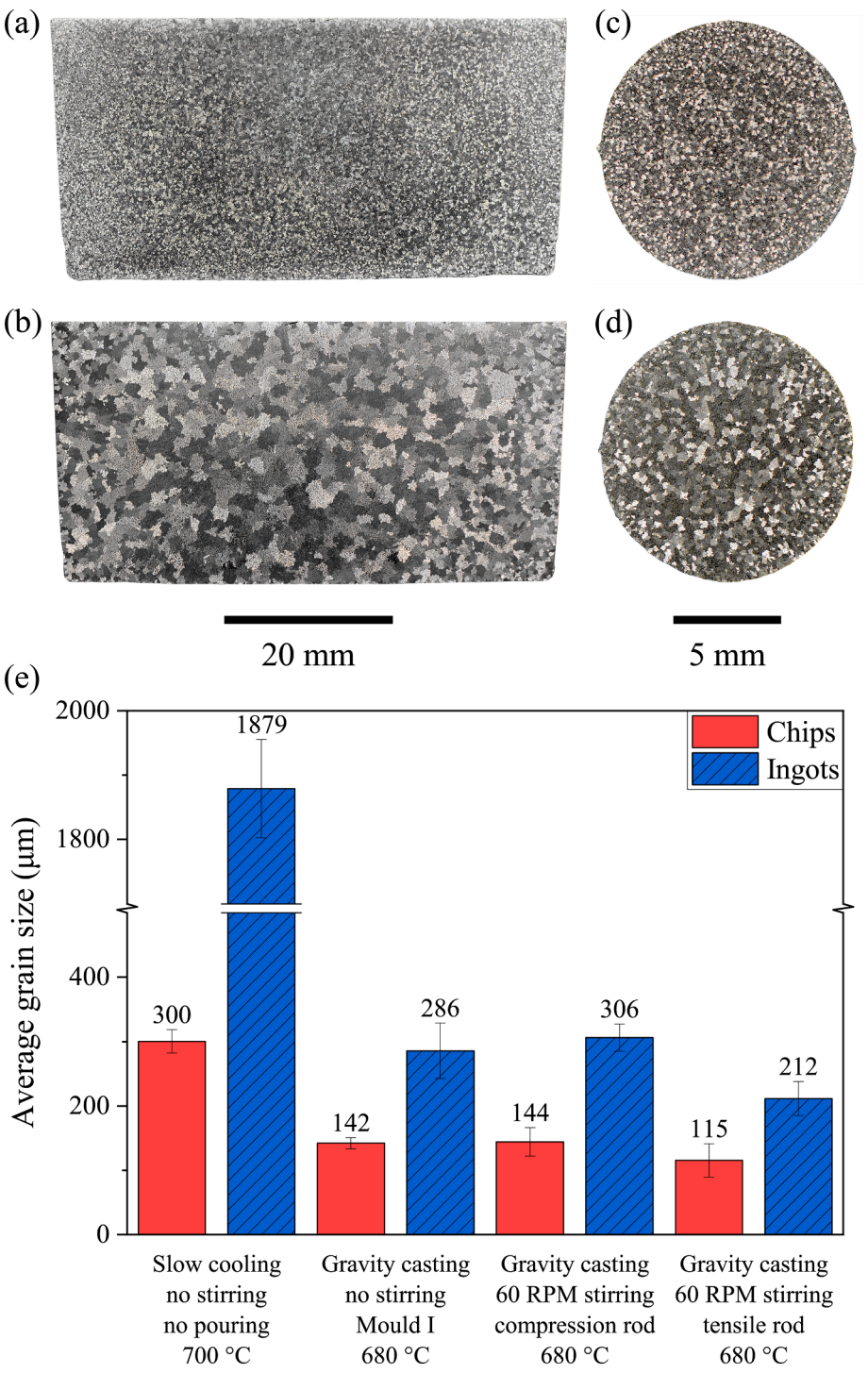


Fig. 2. The micrographs of (a) slow-cooled chip melts, (b) slow-cooled ingot melts, (c) non stirred gravity-cast chip melts in Mould I, and (d) non stirred gravity-cast ingot melts in Mould I. (e) average grain size of samples solidified from chip melts and ingot melts under different solidification conditions.

cooling rate increases, both chips and ingots show a pronounced decrease in T_{min}, as is commonly reported in equiaxed solidification [56–58].

Grain initiation typically requires two conditions: nucleation sites and sufficient undercooling (thermal and/or constitutional). As the melt temperature decreases, the undercooling increases, initiating grain nucleation and growth at nucleation sites, and releasing latent heat. T_{min} is reached when the rate of latent heat release equals the rate of external heat extraction. This is then followed by recalescence where the latent heat flux caused by the growth of grains in the undercooled melt exceeds the external heat flux [59–61].

As shown in Fig. 4(c), during the slow cooling process, chips exhibited a higher T_{min} than ingots, indicating that a sufficient number of nucleation and growth events were activated within a smaller undercooling range. In contrast, at this temperature (T_{min}^{chips}), the rate of latent heat release in the ingot melt was insufficient, causing the melt temperature to continue decreasing. This led to the further growth of existing grains while new grains continued to nucleate. Eventually, at a deeper undercooling, the rate of latent heat release in the ingot melt caught up with the heat extraction rate. Therefore, it was evident that

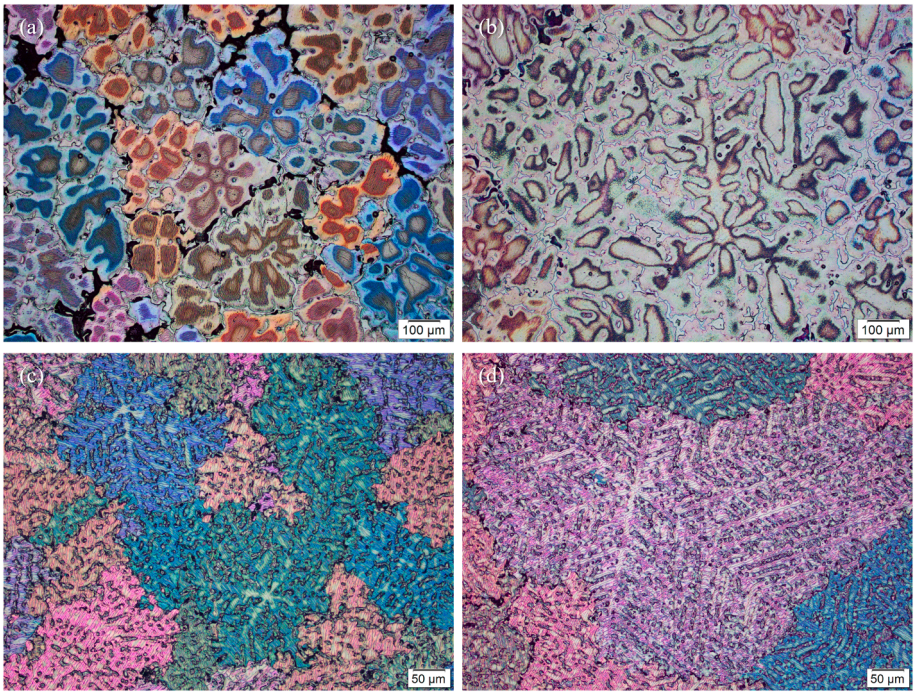


Fig. 3. Optical microscope images of samples solidified from chip melts and ingot melts after colour etching: (a) slow-cooled chip melt, (b) slow-cooled ingot melt, (c) gravity-cast chip melt from Mould I, and (d) gravity-cast ingot melt from Mould I.

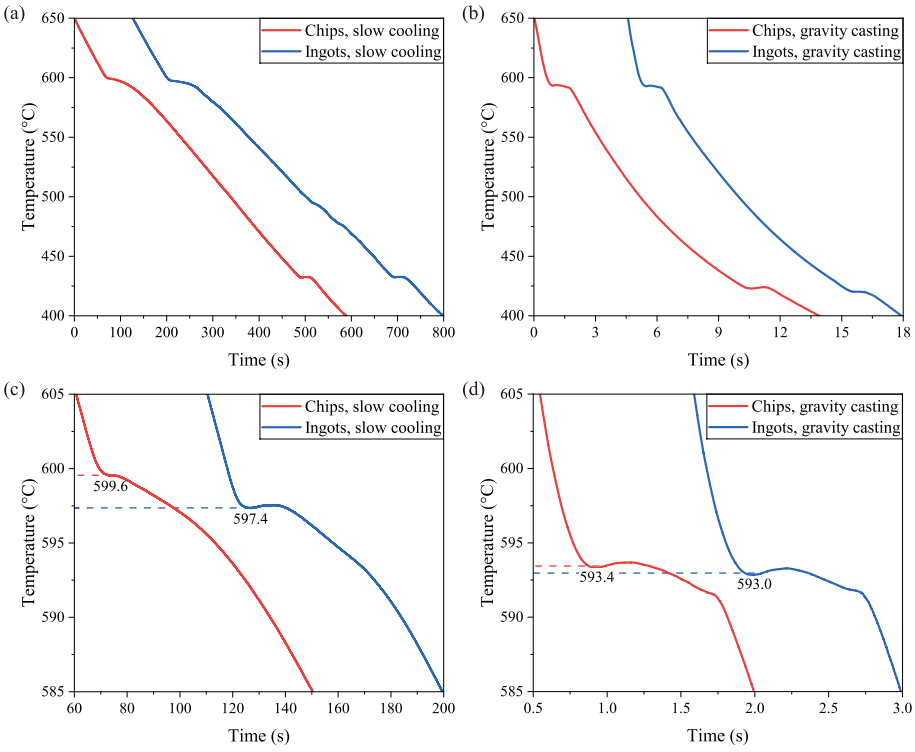


Fig. 4. Cooling curves of (a) (c) slow-cooled samples and (b) (d) gravity castings from Mould I, where (c) and (d) are the zoomed-in early stage (temperature range of 605——585 °C) of α-Mg solidification. In (c) and (d), horizontal lines mark the minimum temperature before recalescence. Curves have been shifted along the time axis to aid the visualisation.

the molten ingots lacked activated nucleation events at a small undercooling while, in chips melts, there was a substantial number of activated nucleation events even at a small undercooling.

In gravity casting, the cooling rate increased by two orders of magnitude compared to slow cooling. Therefore, a deeper undercooling was necessary to increase the number of activated nucleation events and the grain growth rate, enabling the rate of latent heat release to correspondingly increase. As a result, compared to slow cooling, both chip and ingot castings exhibited a significant decrease in T_{min}, leading to more nucleation events and a reduction in grain size (Table 2).

Table 2
Summary of cooling curve parameters, grain size and volumetric grain density, N_v, in castings produced from chip feedstock versus ingot feedstock. S.C. = slow cooling. G.C. = gravity casting.

		Number of samples	Cooling rate (Ks^{-1})	T_{min} (°C)	Recalescence (°C)	Grain size (μm)	N_V (m^{-3})
S.C. no stirring	Chips	6	0.74 ± 0.02	599.55 ± 0.19	0.004 ± 0.001	300 ± 18	1.84E + 10
	Ingots	6	0.72 ± 0.03	597.36 ± 0.72	0.089 ± 0.074	1879 ± 76	7.54E + 7
G.C. no stirring	Chips	6	84.90 ± 5.89	593.45 ± 0.26	0.359 ± 0.012	142 ± 8	1.74E + 11
	Ingots	6	88.43 ± 12.52	592.96 ± 0.13	0.464 ± 0.067	286 ± 43	2.14E + 10

To gain further insights into the link between the measured grain refinement and measured cooling curves, we performed a semi-quantitative analysis within athermal nucleation theory. Following Maxwell and Hellawell [59], Greer [60] and the others [61–63], we assume that recalescence prevents further heterogeneous nucleation events, such that the grain size is determined by the total number of activated nucleation events when the melt temperature reaches T_{min}, which corresponds to the moment of maximum undercooling. We assume that nucleation events occur continuously on cooling following a distribution of nucleation event density versus undercooling. We then explore how this nucleation density distribution differs for chips versus ingots. In literature, a range of distributions have been used for equiaxed solidification including a log-normal [64], Gaussian [65], Weibull [66], and exponential distribution functions [60], and it has been argued that each of these fitting functions approximately resembles each other for the small undercoolings reached during equiaxed solidification [61].

The number of grains per unit volume (N_V) can be estimated from the average grain size (d) measured by the linear intercept method using Eq. (2) [60]. The specific values of N_V for the thermal analysis samples are detailed in Table 2.

$$N_V = \frac{0.5}{d^3}$$

Assuming the nucleation density distribution ($dN_V/d(\Delta T)$ versus ΔT) adheres to a lognormal distribution, as shown in Eq. (3)

$$\frac{dN_V}{d(\Delta T)} = \frac{N_0}{s\Delta T\sqrt{2\pi}}\exp\left(-\frac{[\ln(\Delta T - T_0)]^2}{2s^2}\right)$$

Where N_0, s and T_0 are fitting parameters. Then, N_V versus ΔT follow the lognormal cumulative distribution function (CDF) as described in Eq. (4).

$$N_V = \int_0^{\Delta T} \frac{N_0}{s\Delta T\sqrt{2\pi}}\exp\left(-\frac{[\ln(\Delta T/T_0)]^2}{2s^2}\right)d(\Delta T)$$
$$= N_0\,\mathrm{erf}\left(-\frac{\ln(\Delta T - T_0)}{s}\right)$$

Since the composition and impurities of the melt made from chips in both slow cooling and gravity casting are assumed to be identical, the N_V and T_{min} obtained under these two solidification conditions can be used to fit one cumulative distribution function of the chip melt. After obtaining the fitting values for each parameter, the corresponding CDF and log-normal curves can be plotted. The same approach was then applied to the samples produced from ingots. The nucleation event density and density distribution curves plotted according to the above method are shown in Fig. 5. These fitted curves are a reasonable estimate only within the undercooling range covered by the experimental data.

By comparing the grain density curves in Fig. 5, it is evident that at the same degree of undercooling, the nucleation event density of chips is substantially higher than that of ingots. This discrepancy is especially pronounced when the undercooling is small. Under the slow cooling condition, even when the maximum undercooling of ingots exceeds that of chips by more than 2 °C, the nucleation event density of chips is still approximately 250 times greater than that of ingots. As the liquid cooling rate increases from 0.73 °C/s to 86.7 °C/s, the nucleation event density of chips increases tenfold, while that of ingots increases by over 360 times, reaching approximately one-seventh of chips while maintaining a 0.5 °C undercooling difference. The above analysis indicates that ingot melts are lacking in activatable nucleation sites at small undercooling compared with chip melts. Also, it explains why the grain

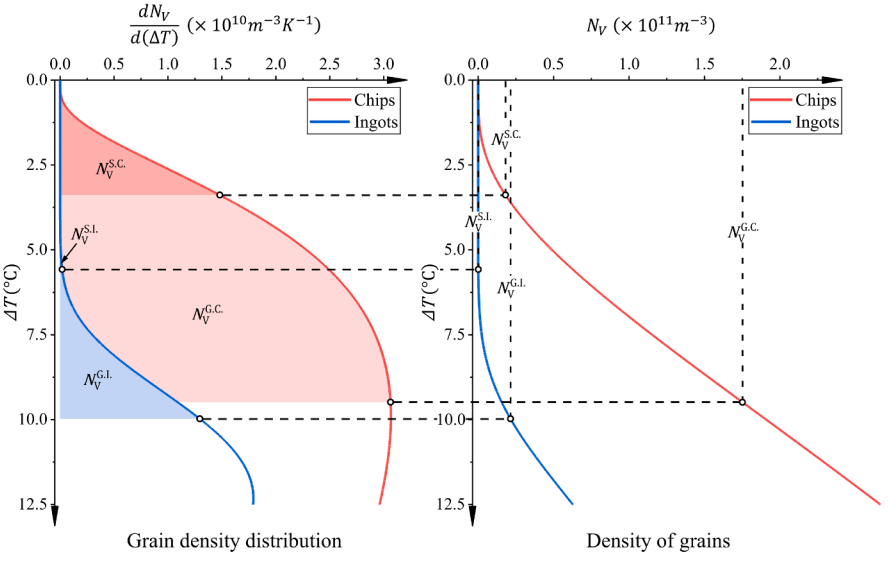


Fig. 5. Nucleation event density and its distribution in chip melts and ingot melts for the cooling curves shown in Fig. 4 (c)-(d). N_v = number of grains per unit volume. Superscripts: S.C. = slow cooled chip melt, S.I. slow cooled ingot melt, G.C. = gravity cast chip melt, G.I. = gravity cast ingot melt.

refinement of chips is less dependent on the cooling rate, as they already possess an ample supply of activatable nucleation events at small undercooling.

Fig. 5 shows that, in order to explain the grain sizes and differences in the cooling curves from chip melts versus ingot melts from a heat flow perspective, it is necessary that melts made from chips contained both a larger number density of nucleation sites and that these sites required a lower undercooling to trigger nucleation events. Considering that one significant difference between chips and ingot feedstock is that chips have a much higher surface-to-volume ratio prior to melting, a natural hypothesis is that chips may introduce more MgO to the melt than ingots and that this MgO may catalyse nucleation. The MgO initially on the chip surfaces is likely to be nanoscale and could contribute to grain refinement in various ways. For example, the MgO introduced may play a role directly as heterogeneous nucleation sites (e.g. [23,67]), or indirectly by restricting the growth of α-Mg dendrites and hindering the diffusion of solute in the liquid (e.g. [68,69]), or both. Further work is required to conclusively prove the mechanism(s) of grain refinement when using chips as feedstock for casting.

3.3. Tensile properties

Fig. 6 compares the tensile properties of chips and ingots in the as-cast state and after T4 solution heat treatment. The engineering stress–strain curves in Fig. 6(a) reveal that, for the as-cast samples, chip samples exhibit slightly higher 0.2 % proof stress, elongation at break, and ultimate tensile strength. T4 heat treatment and quenching result in the dissolution of the hard β-$Mg_{17}Al_{12}$ phase, which decreases the 0.2 % proof stress of both chips and ingot samples, while significantly increasing their ductility. After T4 treatment, the 0.2 % proof stress of chips remains slightly higher than that of ingots, but the elongation of ingot samples slightly surpasses that of the chips. Fig. 6(b) shows that, overall, the tensile properties of chips and ingot samples are similar to each other in both conditions, with no significant decrease in ductility associated with using chips. These results are compared to the yield strength and elongation of gravity-cast AZ91 and AZ80 alloys reported in the literature [70–75], as shown in Table 3. The deviations between different studies may be attributed to the differences in casting processes, solidification conditions, and alloy compositions.

In Fig. 6(b), the 0.2 % proof stress of the as-cast and solution-treated chip samples is respectively 5 % and 1 % higher than that of the ingot samples, attributed to the strengthening effect caused by grain refinement, namely the Hall-Petch effect, represented by Eq. (5).

$$\sigma_y = \sigma_0 + k\frac{1}{\sqrt{d}}$$

where σ_0 and k are constants related to the chemical composition and microstructure of the material. σ_0 includes grain size-independent strengthening effects, and k is responsible for all strengthening effects related to grain size. The physical mechanism of grain boundary strengthening involves the hindering effect of grain boundaries on slip and twining [76–81]. Nevertheless, the enhancement in 0.2 % proof stress introduced by using chips in Fig. 6(b) is rather modest. This is due to the relatively similar grain sizes of tensile specimens made from chips and ingots, as shown in Fig. 2, measuring 115 ± 26 μm and 212 ± 26 μm, respectively. The tensile specimens have the smallest diameter (8.6 mm) among all gravity-cast samples investigated in this study, resulting in the highest cooling rate (higher than 88 Ks^{-1}). According to the analysis in the previous section, at such a high cooling rate, a significant number of nucleation and growth events are activated within the melt of ingots, thereby diminishing the disparity in grain sizes compared to chips.

σ_0 and k are assumed to be the same for ingots and chips, as they both came from exactly the same ingot. Under this assumption, the data points in Fig. 6(c) were fitted. Table 4 enumerates the Hall-Petch slopes

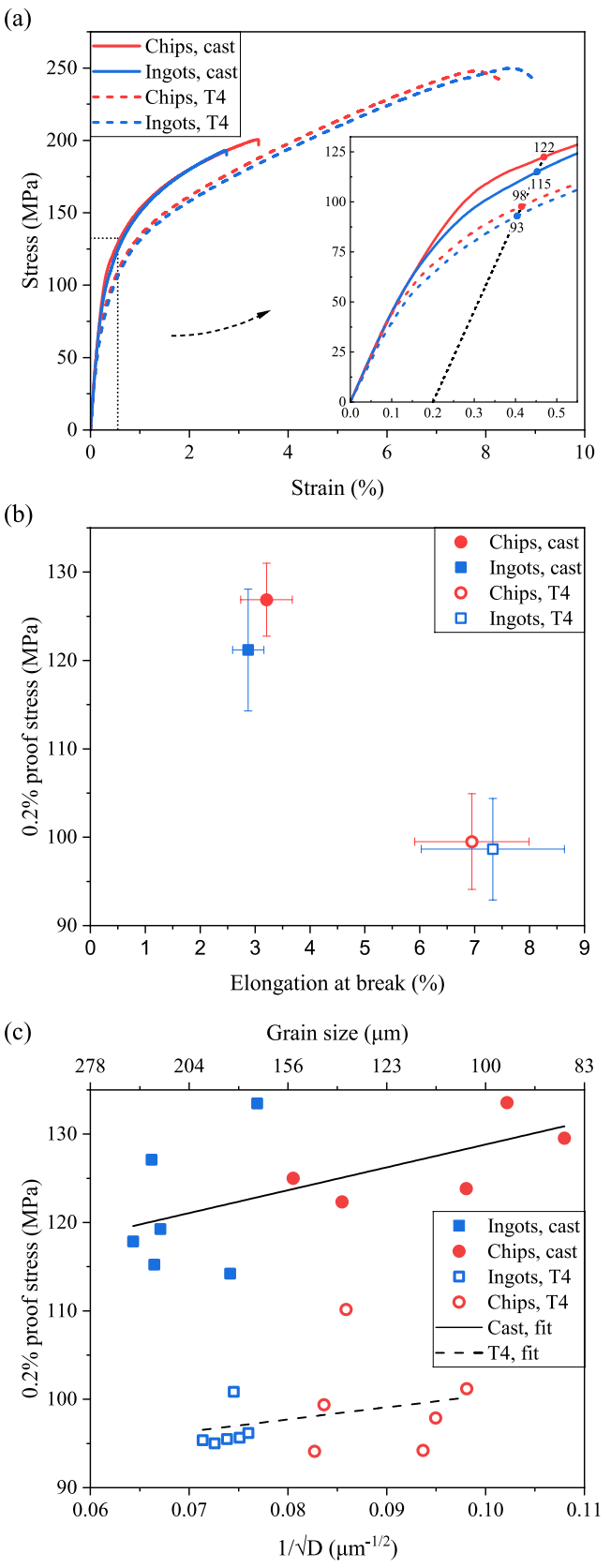


Fig. 6. Tensile properties of as-cast and T4-treated castings made from chip melts and ingot melts: (a) engineering stress–strain curves, (b) scatter plot of the average values of 0.2% proof stress against elongation at break. Error bars represent the standard deviation of six samples, (c) scatter plot of 0.2% proof stress against grain size.

Table 3
Tensile properties of gravity cast AZ91 and AZ80 alloys.

Reference	Material	Condition	Yield strength (MPa)	Elongation (%)
This work	AZ91/AZ80 chip	Cast	126.9 ± 4.1	3.2 ± 0.5
This work	AZ91/AZ80 ingot	Cast	121.2 ± 6.9	2.9 ± 0.3
[70]	AZ91	Cast	85	1.7
[71]	AZ91	Cast	95	2.1
[72]	AZ91	Cast	78 ± 3.8	1.9 ± 0.2
[73]	AZ80	Cast	71 ± 0.5	3.6 ± 0.5
[74]	AZ80	Cast	117.3 ± 10.5	16.2 ± 5.9
This work	AZ91/AZ80 chip	T4	99.5 ± 5.4	6.9 ± 1.0
This work	AZ91/AZ80 ingot	T4	98.6 ± 5.7	7.3 ± 1.3
[75]	AZ91	T4	91 ± 6	11 ± 2
[74]	AZ80	T4	117.2 ± 1.6	29.8 ± 0.1

Table 4
The Hall-Petch slopes (k) of AZ91 alloys under various processing conditions.

Reference	Processing	d (μm)	k (MPa μm$^{1/2}$)
This work	Gravity casting	86–242	200
This work	Solution treatment	104–239	137
[83]	Rheocasting	50–191	194
[84]	Rapid solidification	0.3–5000	210
[85]	Extrusion	1–100	244
[85]	Equal-channel angular extrusion	1–100	138
[86]	Extrusion, equal-channel angular pressing	1–1000	250

(k) alongside corresponding values from the literature. The value of k depends on the deformation mode (including basal slip, prismatic slip, pyramidal $\langle a \rangle$ slip, pyramidal $\langle c+a \rangle$ slip, $\{10\bar{1}2\}$ twinning and $\{10\bar{1}1\}$ twinning), which is influenced by many factors such as processing conditions and grain size [82]. Table 4 shows that the k values in this study are largely consistent with those in the literature with similar processing conditions and grain size ranges. Furthermore, a decrease in the k value was observed after solid solution treatment, which can be attributed to the dissolution of the β-$Mg_{17}Al_{12}$ phase after the heat treatment, reducing the dislocation pinning sites and thus lowering the critical resolved shear stress (CRSS), thereby facilitating dislocation slip.

In Fig. 6(b), the tensile specimens of chips and ingots exhibit similar elongation at break. Fractography was conducted on the tensile specimens to investigate the fracture mechanism. Using a stereo microscope, symmetric dark regions and ellipsoidal pores were sometimes observed on both sides of the tensile samples. Example samples with serious defects are presented in Fig. 7. As shown in Fig. 8(a)-(d), the dark regions on the fracture surface under visible light correspond to the bright regions in the SEM images detected using secondary electrons. EDX analysis indicates that this is a layer of MgO. Combining the symmetric features observed in Fig. 7, it can be confirmed that these are double oxide films, a typical entrainment defect formed by folding the surface oxide into the melt interior during the casting process, which results in a nonbonded interface equivalent to a pre-existing crack [35,39,87–89].

Fig. 8(a) to (d) show that the brown features observed under the stereo microscope are essentially entrained oxides, manifesting as either dendrites covered by oxide films or as clusters of nanoscale MgO particles. From Fig. 8(c) and (e), it can be seen that these oxide films are rough at the nanoscale, with roughness increasing alongside their thickness. Besides the brown features, gas bubbles are another common form of defects on the fracture surfaces. The macroscopic and microscopic morphologies of the millimetre-sized bubbles are shown in Fig. 7 and Fig. 8(f), respectively. In Fig. 8(f), creases formed by the stretching

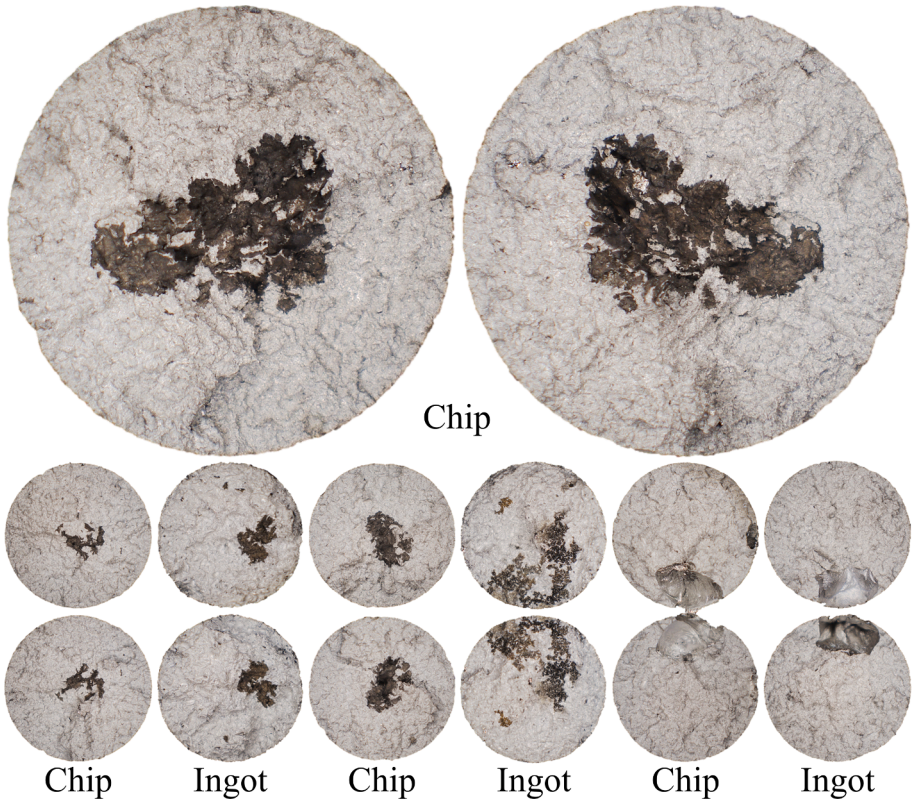


Fig. 7. Oxide film defects (dark regions) and gas pores (last two pairs) on seven pairs of fracture surfaces of the tensile specimens. The diameter of the tensile rods is 8.6 mm.

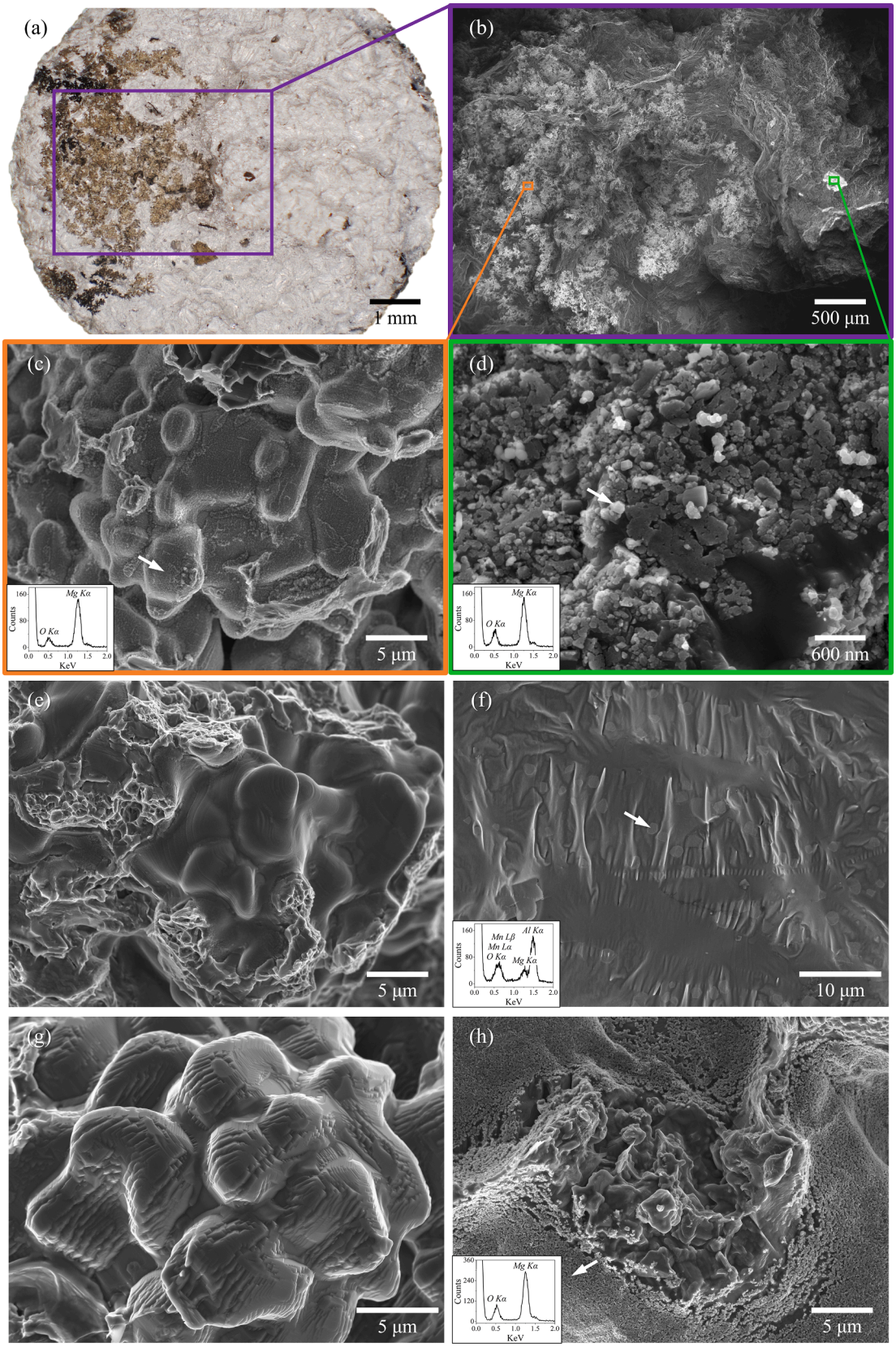


Fig. 8. Fractography of the tensile specimens, where (a)-(d) are from a solution-treated chip sample, (e) and (f) from as-cast chip samples, and (g) and (h) from as-cast ingot samples. (a) Stereo micrograph, (b) SEM image obtained in Inlens mode, (c) α-Mg dendrites covered by a thick oxide film, (d) clusters of nanoscale oxide particles, (e) α-Mg dendrites covered by a thin oxide film, (f) the surface of a large ellipsoidal pore (from the second-to-last pair of samples of Fig. 7) with many Al_8Mn_5 particles adhering to the wet side of the oxide film, (g) clean α-Mg dendrites without any discernible oxide film, (h) α-Mg dendrites covered by a thick oxide film, where MgO nanoparticles can be seen.

of oxide films can be observed on the surface of the bubbles. Al_8Mn_5 particles can also be observed on the wet side of these bubbles as indicated by a white arrow in Fig. 8(f), which is common in AZ91 castings [37,90,91]. These defects are present in both chip and ingot samples. Fig. 8(g) and (h) display the as-cast ingot samples with clean α-Mg dendrites without any oxide film and α-Mg dendrites covered by a thick oxide film, respectively.

Based on the fractography, two predominant casting defect types were identified, dark oxide films and gas pores. The area fraction of defects on the fracture surface was measured as the total projected area of the two types of defects. Fig. 9(a) compares the area fraction of defects on the fracture surface (averaged over both sides) with the volumetric porosity of each tensile specimen measured by the Archimedes method. There is no significant correlation between the two, which is attributed to the largest casting defects being localized with insignificant impact on the overall density. Further analysis of the impact of volumetric porosity on the fracture elongation of tensile specimens, as shown in Fig. 9(b), reveals a weak negative correlation between the two. In contrast, the elongation at break of the specimens demonstrates a stronger negative correlation with the area fraction of defects on the fracture surface, as depicted in Fig. 9(c). This suggests that the fracture elongation of both chip and ingot samples is rather determined by the area fraction of defects on the fracture surface. This observation aligns with conclusions from previous literature on castings [39,92–95]. Moreover, the scatter plots for chip and ingot samples overlap, indicating that similar distributions of casting defect area fraction exist on the fracture surfaces in both chip and ingot samples and result in similar elongation in each type of sample.

Both the oxide film defects and gas bubbles on the fracture surfaces are entrainment defects, which were introduced into the melt during the stirring and pouring processes [89]. This suggests that the fracture elongation of the tensile specimens in this study was primarily governed by the casting process and mould design, regardless of whether the initial material was in the form of chips or ingots. The fracture elongation of the tensile specimens primarily reflected the casting defects' severity instead of the performance differences between chips and ingots (as well as their grain sizes). This also shows that the difference in ductility between chips and ingot castings is very small because it is overshadowed by the influence of casting defects.

To summarise, chip castings show a slight improvement in yield strength compared to castings from ingots, without compromising their elongation at break.

4. Conclusions

This study has demonstrated the feasibility of recycling AZ91/AZ80 machining chips through shape casting. A novel finding is that chip castings display significant grain refinement (up to 84 %), and their tensile performance remains unharmed and can be even improved by the grain refinement. The main conclusions are as follows:

- Casting using chips as feedstock, as opposed to ingots, led to substantial grain refinement. The grain size in chip castings was 1/6 to 1/2 of that in ingots when the liquid cooling rate ranged from 0.73 °C/s to 86.7 °C/s, with a more pronounced difference at slower cooling rates.
- The cooling curves clearly indicated that, at the same undercooling, the nucleation event density in the chip melt was always higher than in the ingot melt. The difference in nucleation event density between chips and ingots was particularly significant at a small undercooling.
- Castings from chips and ingots displayed similar tensile performance in both as-cast and solution heat-treated conditions. Chip samples had a slightly higher 0.2 % proof stress than that of ingot samples (up to 5 %), aligning with the Hall-Petch effect in the literature. Fracture elongation for both chips and ingots was comparable, primarily

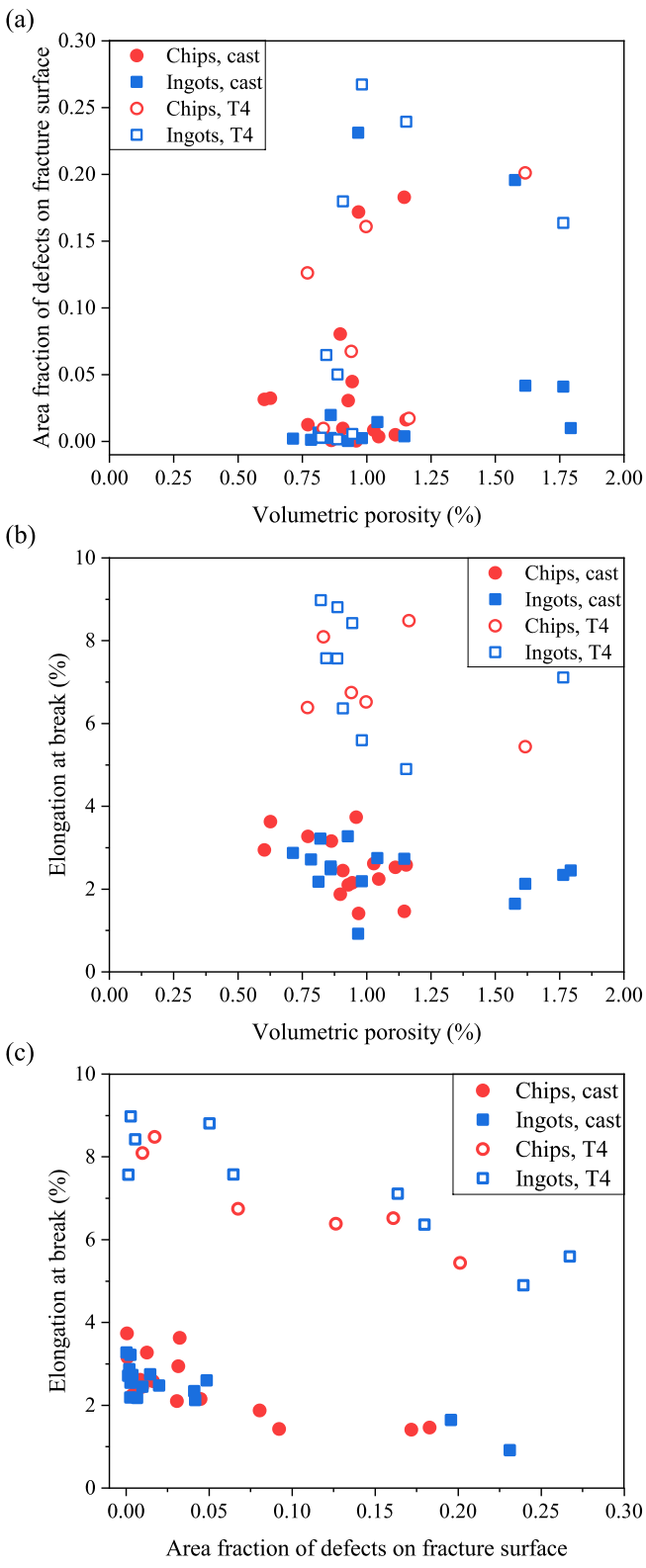


Fig. 9. Correlations between elongation at break and microstructural factors: (a) relationship between area fraction of defects on the fracture surface and volumetric porosity, (b) elongation at break versus volumetric porosity, (c) elongation at break versus area fraction of defects on the fracture surface.

influenced by the area fraction of defects on the fracture surface introduced during the pouring process.
- The original oxides on the chip surface did not negatively impact the castings' ductility. Further research is needed to determine whether there is a connection between these oxides and the grain refinement effect of chips.

CRediT authorship contribution statement

Xinyi Hao: Writing – original draft, Methodology, Investigation, Formal analysis, Data curation. **Zhuocheng Xu:** Writing – review & editing, Methodology. **Christopher M. Gourlay:** Writing – review & editing, Supervision, Methodology, Investigation. **Qianqian Li:** Writing – review & editing, Supervision, Methodology, Investigation.

Declaration of competing interest

The authors declare that they have no known competing financial interests or personal relationships that could have appeared to influence the work reported in this paper.

Data availability

Data will be made available on request.

Acknowledgements

The authors gratefully acknowledge the use of characterisation facilities within the Harvey Flower Electron Microscopy Suite, Department of Materials, Imperial College London.

References

[1] S. Rahimpour Golroudbary, I. Makarava, A. Kraslawski, Environmental assessment of global magnesium production, Miner. Process. Extr. Metall. Rev. 44 (6) (2023) 389–406.
[2] G. Liu, Y. Wang, Z. Fan, A physical approach to the direct recycling of Mg-alloy scrap by the rheo-diecasting process, Mater. Sci. Eng. A 472 (1–2) (2008) 251–257.
[3] J. Tan, S. Ramakrishna, Applications of magnesium and its alloys: A review, Appl. Sci. 11 (15) (2021) 6861.
[4] F. Bella, et al., An overview on anodes for magnesium batteries: Challenges towards a promising storage solution for renewables, Nanomaterials 11 (3) (2021) 810.
[5] L.M. Calado, M.J. Carmezim, M.F. Montemor, Rare earth based magnesium alloys—a review on WE series, Front. Mater. 8 (2022) 804906.
[6] V.V. Ramalingam, et al., Research and development in magnesium alloys for industrial and biomedical applications: a review, Met. Mater. Int. 26 (2020) 409–430.
[7] *B94 Standard Specification for Magnesium-Alloy Die Castings*. 2018.
[8] *B90/B90M Standard Specification for Magnesium-Alloy Sheet and Plate*. 2015.
[9] B. Liu, et al., Development and application of magnesium alloy parts for automotive OEMs: A review, J. Magnesium Alloys 11 (1) (2023) 15–47.
[10] A. Dziubinska, et al., Review of Magnesium Wheel Types and Methods of Their Manufacture, Materials 17 (3) (2024) 584.
[11] P. Oslanec, K. Iždinský, F. Simančík, Possibilities of magnesium recycling, Mater. Sci. Technol. 4 (2008) 83–88.
[12] G. Hanko, H. Antrekowitsch, P. Ebner, Recycling Automotive Magnesium Scrap, Jom 54 (2002) 51–54.
[13] M. Mabuchi, K. Kubota, K. Higashi, New recycling process by extrusion for machined chips of AZ91 magnesium and mechanical properties of extruded bars, Mater. Trans. JIM 36 (10) (1995) 1249–1254.
[14] Y.Q. Li, et al., Recent research and advances in extrusion forming of magnesium alloys: A review, J. Alloy. Compd. (2023) 170080.
[15] S. Shamsudin, M. Lajis, Z.W. Zhong, Solid-state recycling of light metals: A review, Adv. Mech. Eng. 8 (8) (2016), 1687814016661921.
[16] L. Chen, et al., Microstructural evolution in graphene nanoplatelets reinforced magnesium matrix composites fabricated through thixomolding process, J. Alloy. Compd. 940 (2023) 168824.
[17] Avedesian, M.M., H. Baker, *ASM specialty handbook: magnesium and magnesium alloys*. Vol. 274. 1999: ASM international Materials Park, OH.
[18] M. Rakshith, P. Seenuvasaperumal, Review on the effect of different processing techniques on the microstructure and mechanical behaviour of AZ31 Magnesium alloy, J. Magnesium Alloys 9 (5) (2021) 1692–1714.
[19] T. Davis, L. Bichler, Effect of Al-Ti master alloy on the grain refinement and hot tearing of AZ91 Mg alloys, J. Mater. Eng. Perform. 32 (6) (2023) 2577–2586.
[20] C. Sager, et al., Physical metallurgy of Mg AZ80 alloys for forging applications, Mater. Soc. Annu. Meet 12 (2009) 405–410.
[21] X. Chen, et al., Comparison study of hot deformation behavior and processing map of AZ80 magnesium alloy casted with and without ultrasonic vibration, J. Alloy. Compd. 803 (2019) 585–596.
[22] X. Chen, et al., The hot rolling deformation performance of as-cast AZ80 magnesium alloy after ultrasonic processing, J. Mater. Res. Technol. 17 (2022) 1707–1715.
[23] Z. Fan, et al., Grain refinement of Mg-alloys by native MgO particles: An overview, J. Magnesium Alloys (2022).
[24] A.P. Carvalho, R.B. Figueiredo, An overview of the effect of grain size on mechanical properties of magnesium and its alloys, Mater. Trans. 64 (7) (2023) 1272–1283.
[25] H. Mirzadeh, Grain refinement of magnesium alloys by dynamic recrystallization (DRX): A review, J. Mater. Res. Technol. (2023).
[26] K. Ralston, N. Birbilis, C. Davies, Revealing the relationship between grain size and corrosion rate of metals, Scr. Mater. 63 (12) (2010) 1201–1204.
[27] M. Liang, et al., Effects of rare earth neodymium (Nd) and heat treatment on anti-corrosion behaviors of the AZ80 magnesium alloy, Adv. Compos. Hybrid Mater. 5 (2) (2022) 1460–1476.
[28] Y. Ali, et al., Current research progress in grain refinement of cast magnesium alloys: A review article, J. Alloy. Compd. 619 (2015) 639–651.
[29] M. Sun, et al., Recent advances in the grain refinement effects of Zr on Mg alloys: a review, Metals 12 (8) (2022) 1388.
[30] Z. Liu, Review of grain refinement of cast metals through inoculation: theories and developments, Metall. Mater. Trans. A 48 (2017) 4755–4776.
[31] E. Karakulak, A review: Past, present and future of grain refining of magnesium castings, J. Magnesium Alloys 7 (3) (2019) 355–369.
[32] G. Wu, et al., Recent advances on grain refinement of magnesium rare-earth alloys during the whole casting processes: A review, J. Magnesium Alloys (2023).
[33] Z. Fan, et al., Enhanced heterogeneous nucleation in AZ91D alloy by intensive melt shearing, Acta Mater. 57 (16) (2009) 4891–4901.
[34] W. Griffiths, N.-W. Lai, Double oxide film defects in cast magnesium alloy, Metall. Mater. Trans. A 38 (2007) 190–196.
[35] Wang, L., et al. *Oxide Film and Porosity Defects in Magnesium Alloy AZ91*. in *Shape Casting: 3rd Intern. Symp*. 2009.
[36] S. Lun Sin, A. Elsayed, C. Ravindran, Inclusions in magnesium and its alloys: a review, Int. Mater. Rev. 58 (7) (2013) 419–436.
[37] D. Mackie, et al., Characterisation and modelling of defect formation in direct-chill cast AZ80 alloy, Mater Charact 104 (2015) 116–123.
[38] M.M. Jalilvand, et al., On the dynamically formed oxide films in molten Mg, J. Magnesium Alloys 8 (1) (2020) 219–230.
[39] T. Li, J. Davies, X. Zhu, Effect of carrier gases on the entrainment defects within AZ91 alloy castings, J. Magnesium Alloys 10 (1) (2022) 129–145.
[40] M.M. Jalilvand, et al., Surface oxidation study of molten Mg–Al alloys by oxide/metal/oxide sandwich method, J. Magnesium Alloys 10 (6) (2022) 1704–1717.
[41] *BS EN ISO 4497:2020: Metallic powders. Determination of particle size by dry sieving*. 2020, British Standards Institute.
[42] B. Davis, et al., Study of chip morphology and chip formation mechanism during machining of magnesium-based metal matrix composites, J. Manuf. Sci. Eng. 139 (9) (2017) 091008.
[43] *B661 Standard Practice for Heat Treatment of Magnesium Alloys*. 2012.
[44] *B962 Standard Test Methods for Density of Compacted or Sintered Powder Metallurgy (PM) Products Using Archimedes' Principle*. 2017.
[45] *B557M Standard Test Methods for Tension Testing Wrought and Cast Aluminum- and Magnesium-Alloy Products (Metric)*. 2015.
[46] A. Maltais, et al., Improvements in the metallography of as-cast AZ91 alloy, Mater Charact 52 (2) (2004) 103–119.
[47] *E112 Standard Test Methods for Determining Average Grain Size*. 2013.
[48] E. Vandersluis, C. Ravindran, Comparison of measurement methods for secondary dendrite arm spacing, Metallograp., Microstruct. Anal. 6 (2017) 89–94.
[49] W. Kurz, D. Fisher, Secondary spacing after directional or equiaxed growth, Fundam. Solidif (1984) 88–93.
[50] K. Pettersen, O. Lohne, N. Ryum, Dendritic solidification of magnesium alloy AZ91, Metall. Trans. A 21 (1990) 221–230.
[51] C. Labrecque, et al., Inverted disk centrifugal atomization of AZ91 magnesium alloy, Can. Metall. Q. 36 (3) (1997) 169–175.
[52] D. Dubé, et al., Secondary dendrite arm spacings in magnesium alloy AZ91D: from plaster moulding to laser remelting, Int. J. Cast Met. Res. 11 (3) (1998) 139–144.
[53] Kim, J., M. Isac, and R. Guthrie, *Metal-mold heat transfer and solidification of magnesium alloys in belt casting processes*. Proceed. Magnes. Technol. (TMS'04), 2004: p. 247-257.
[54] M. Paliwal, et al., The evolution of as-cast microstructure of ternary Mg-Al-Zn alloys: an experimental and modeling study, Metall. Mater. Trans. A 45 (2014) 3596–3608.
[55] C.-J. Lin, et al., Eutectic solidification in Mg-9Al-0.7 Zn: From divorced to coupled growth, J. Alloy. Compd. 938 (2023) 168571.
[56] P. Thevoz, J. Desbiolles, M. Rappaz, Modeling of equiaxed microstructure formation in casting, Metall. Trans. A 20 (1989) 311–322.
[57] Ø. Grong, et al., Analytical modelling of equiaxed solidification, Acta Mater. 46 (14) (1998) 5045–5052.
[58] E. Fraś, et al., Theoretical model for heterogeneous nucleation of grains during solidification, Mater. Sci. Technol. 19 (12) (2003) 1653–1660.
[59] I. Maxwell, A. Hellawell, A simple model for grain refinement during solidification, Acta Metall. 23 (2) (1975) 229–237.

[60] A. Greer, et al., Modelling of inoculation of metallic melts: application to grain refinement of aluminium by Al–Ti–B, Acta Mater. 48 (11) (2000) 2823–2835.
[61] J. Lelito, et al., Effect of SiC reinforcement particles on the grain density in a magnesium-based metal–matrix composite: Modelling and experiment, Acta Mater. 60 (6–7) (2012) 2950–2958.
[62] M.A. Martorano, D.T. Aguiar, J.M.R. Arango, Multigrain and multiphase mathematical model for equiaxed solidification, Metall. Mater. Trans. A 46 (2015) 377–395.
[63] Y. Xu, et al., Revealing the heterogeneous nucleation behavior of equiaxed grains of inoculated Al alloys during directional solidification, Acta Mater. 149 (2018) 312–325.
[64] T.E. Quested, A.L. Greer, The effect of the size distribution of inoculant particles on as-cast grain size in aluminium alloys, Acta Mater. 52 (13) (2004) 3859–3868.
[65] Thévoz, P., et al., *Modelling of equiaxed dendritic and eutectic growth in castings*. 1987, Institute of Metals.
[66] E. Fras, et al., Theoretical model for heterogeneous nucleation of grains during solidification, Mater. Sci. Technol. 19 (12) (2003) 1653.
[67] G. Shen, et al., The first principle research of CaO and MgO particulate heterogeneous nucleation in Mg alloys, Appl. Surf. Sci. 593 (2022) 153224.
[68] E. Guo, et al., The influence of nanoparticles on dendritic grain growth in Mg alloys, Acta Mater. 152 (2018) 127–137.
[69] H. Li, et al., Nanoparticle-induced growth behavior of primary α-Mg in AZ91 alloys, Mater. Des. 196 (2020) 109146.
[70] G. Wu, et al., The effect of Ca and rare earth elements on the microstructure, mechanical properties and corrosion behavior of AZ91D, Mater. Sci. Eng. A 408 (1–2) (2005) 255–263.
[71] Y. Turen, Effect of Sn addition on microstructure, mechanical and casting properties of AZ91 alloy, Mater. Des. 49 (2013) 1009–1015.
[72] H. Shastri, et al., Microstructural correlation with tensile and creep properties of AZ91 alloy in three casting techniques, J. Manuf. Process. 57 (2020) 566–573.
[73] X. Zhao, et al., Microstructure Evolution and Mechanical Properties of AZ80 Mg Alloy during Annular Channel Angular Extrusion Process and Heat Treatment, Materials 12 (24) (2019) 4223.
[74] B. Pargavi, S.,, et al., Mechanical, electrochemical corrosion, and high-temperature oxidation properties of stir-cast and heat-treated AZ80 magnesium alloy, Mater. Today Commun. 38 (2024) 108181.
[75] C. Caceres, et al., Effects of solidification rate and ageing on the microstructure and mechanical properties of AZ91 alloy, Mater. Sci. Eng. A 325 (1–2) (2002) 344–355.
[76] B. Leu, et al., Twinning pathways enabled by precipitates in AZ91, Materialia 21 (2022) 101292.
[77] S.R. Kada, et al., In-situ X-ray diffraction studies of slip and twinning in the presence of precipitates in AZ91 alloy, Acta Mater. 119 (2016) 145–156.
[78] J.D. Robson, N. Stanford, M.R. Barnett, Effect of precipitate shape on slip and twinning in magnesium alloys, Acta Mater. 59 (5) (2011) 1945–1956.
[79] S.-G. Hong, S.H. Park, C.S. Lee, Role of 10–12 twinning characteristics in the deformation behavior of a polycrystalline magnesium alloy, Acta Mater. 58 (18) (2010) 5873–5885.
[80] M. Barnett, Twinning and the ductility of magnesium alloys: Part I:"Tension" twins, Mater. Sci. Eng. A 464 (1–2) (2007) 1–7.
[81] Q. Chen, et al., The mechanisms of grain growth of Mg alloys: a review, J. Magnesium Alloys 10 (9) (2022) 2384–2397.
[82] H. Yu, et al., Hall-Petch relationship in Mg alloys: A review, J. Mater. Sci. Technol. 34 (2) (2018) 248–256.
[83] H.-M. Guo, et al., Refining microstructure of AZ91 magnesium alloy by introducing limited angular oscillation during initial stage of solidification, Mater. Sci. Eng. A 532 (2012) 221–229.
[84] G. Nussbaum, et al., Strengthening mechanisms in the rapidly solidified AZ 91 magnesium alloy, Scr. Metall. 23 (7) (1989) 1079–1084.
[85] M. Mabuchi, et al., The grain size and texture dependence of tensile properties in extruded Mg-9Al-1Zn, Mater. Trans. 42 (7) (2001) 1182–1188.
[86] M.M. Castro, et al., Inverse Hall-Petch Behaviour in an AZ91 Alloy and in an AZ91–Al2O3 Composite Consolidated by High-Pressure Torsion, Adv. Eng. Mater. 22 (10) (2020) 1900894.
[87] A. Mirak, et al., Effect of oxide film defects generated during mould filling on mechanical strength and reliability of magnesium alloy castings (AZ91), Int. J. Cast Met. Res. 25 (3) (2012) 188–194.
[88] A. Mirak, et al., Oxide film characteristics of AZ91 magnesium alloy in casting conditions, Int. J. Cast Met. Res. 20 (4) (2007) 215–220.
[89] J. Campbell, Chapter 2 - Entrainment, in: J. Campbell (Ed.), Castings (second Edition), Butterworth-Heinemann, Oxford, 2003, pp. 17–69.
[90] L. Peng, et al., Al 8 Mn 5 Particle Settling and Interactions with Oxide Films in Liquid AZ91 Magnesium Alloys, JOM 71 (2019) 2235–2244.
[91] L. Peng, et al., Al-Mn intermetallics in high pressure die cast AZ91 and direct chill cast AZ80, Metals 12 (2) (2022) 266.
[92] C. Caceres, B. Selling, Casting defects and the tensile properties of an AlSiMg alloy, Mater. Sci. Eng. A 220 (1–2) (1996) 109–116.
[93] S. Lee, et al., Quantitative fractographic analysis of variability in the tensile ductility of high-pressure die-cast AE44 Mg-alloy, Mater. Sci. Eng. A 427 (1–2) (2006) 255–262.
[94] Z. Li, et al., Characterization on the formation of porosity and tensile properties prediction in die casting Mg alloys, J. Magnesium Alloys 10 (7) (2022) 1857–1867.
[95] H. Song, et al., Research on the formation mechanism and fracture behavior of bifilm defects, J. Mater. Res. Technol. 26 (2023) 6919–6927.